PHYSICAL REVIEW B **96**, 045108 (2017)

Site-specific spin crossover in Fe_2TiO_4 post-spinel under high pressure up to nearly a megabar

W. M. Xu,[1,*] G. R. Hearne,[2] S. Layek,[1] D. Levy,[1] J-P. Itié,[3] M. P. Pasternak,[1] G. Kh. Rozenberg,[1] and E. Greenberg[1,4]
[1]*School of Physics and Astronomy, Tel Aviv University, 69978 Tel Aviv, Israel*
[2]*Department of Physics, University of Johannesburg, P.O. Box 524, Auckland Park, 2006, Johannesburg, South Africa*
[3]*Synchrotron SOLEIL, L'Orme des Merisiers, Saint-Aubin, BP 48, 91192 Gif-sur-Yvette Cedex, France*
[4]*Center for Advanced Radiation Sources, University of Chicago, Argonne, Ilinois 60439, USA*

(Received 1 May 2017; published 10 July 2017)

X-ray diffraction studies to ~90 GPa at room temperature show that Fe_2TiO_4 ferrous inverse spinel undergoes the following sequence of structural transitions: cubic ($Fd\bar{3}m$) $\xrightarrow{\sim 8\text{ GPa}}$ tetragonal ($I4_1/amd$) $\xrightarrow{\sim 16\text{ GPa}}$ orthorhombic ($Cmcm$) $\xrightarrow{\sim 55\text{ GPa}}$ orthorhombic ($Pmma$), at the indicated onset transition pressures. Within the $Cmcm$ phase, site-specific spin crossover is initiated and involves only highly distorted octahedral sites constituting ~25% of all Fe locations. This is manifest as a steeper volume decrease of $\Delta V/V_0 \sim 3.5\%$ beyond ~40 GPa and an emergent diamagnetic component discerned in ^{57}Fe Mössbauer spectroscopy at variable cryogenic temperatures. A subsequent $Cmcm \rightarrow Pmma$ Fe/Ti disorder-order reconfiguration is facilitated at sixfold coordinated (octahedral) sites. The rest of the high-spin Fe in sixfold and eightfold coordinated sites (~75% abundance) in the $Pmma$ phase exhibit average saturation internal magnetic fields of $H_{hf} \sim 42$ T to ~90 GPa, typical of spin-only (orbitally quenched) Fermi-contact values. By contrast, average $H_{hf} \sim 20$ T values, signifying unquenched orbital moments, occur below the 40–45 GPa spin-crossover initiation regime in the $Cmcm$ phase. Therefore, site-specific spin crossover invokes a cooperative lattice response and polyhedral distortions at the rest of the high-spin Fe sites, translating to 3d level (sub-band) changes and consequential orbital moment quenching. Near ~90 GPa, Fe_2TiO_4 is a partially spin-converted chemically ordered $Pmma$ post-spinel having a persistent charge gap of ~100 meV. Despite structural symmetry changes, partial spin crossover and lattice compressibility, resulting in a ~33% total reduction in unit-cell volume and corresponding 3d bandwidth broadening, strong electron correlations persist at high densification.

DOI: 10.1103/PhysRevB.96.045108

I. INTRODUCTION

Ulvöspinel, Fe_2TiO_4, is a 2-4 inverse spinel comprising ferrous ions which occupy both tetrahedral (A) sites and octahedral (B) sites. Fe^{2+} and Ti^{4+} cations are disordered on the B sublattice, and the spinel formulation may be rendered as follows: $Fe^{2+}(Fe^{2+}Ti^{4+})O_4$ [1,2], where the cations inside the parentheses occupy octahedral B sites and those outside occupy tetrahedral A sites. At ambient conditions, Fe_2TiO_4 is cubic (space group (SG) $Fd\bar{3}m$). It transforms to the tetragonal phase (SG $I4_1/amd$) below 163 K due to a Jahn-Teller distortion associated with Fe^{2+} at the tetrahedral sites [1]. The onset of antiferromagnetism occurs at $T_N \sim 136$ K from the opposing spin alignments on A and B sublattices. Appreciable distortions occur along crystallographic directions in the magnetically ordered state. Both this giant magnetostriction and increases in magnetocrystalline anisotropy are attributed to an important role of tetrahedral Fe^{2+} and associated Jahn-Teller effects [3–6].

Of no less importance or interest is that ulvöspinel is an end member of the important titanomagnetite solid solution between Fe_3O_4 (magnetite) and Fe_2TiO_4. Compositions of titanomagnetite are the dominant carrier of magnetic remanence in nature and have central importance to paleomagnetic, rock magnetic, and mineral magnetic studies [7,8]. Titanomagnetite solid solutions may be formulated as $Fe_{3\text{-}x}Ti_xO_4$, where x defines the proportion of ulvöspinel in the solid solution. The distribution of Fe^{2+}, Fe^{3+}, and Ti^{4+} cations is of crucial importance in determining the magnetic properties pertinent to rock magnetism. Whereas antiferromagnetic Fe_2TiO_4 has spin-compensating octahedral and tetrahedral sublattices, magnetite $Fe^{3+}(Fe^{2+}Fe^{3+})O_4$ in turn is a well-known ferrimagnet with $T_C \sim 860$ K. Moreover, the magnetostriction and magnetocrystalline anisotropy mentioned above for Fe_2TiO_4 also occur in the solid solution series $Fe_{3\text{-}x}Ti_xO_4$, and the extent of these magnetic responses are positively dependent on the ulvöspinel content [9,10].

Extensive high-pressure studies have already been conducted on the one end member, magnetite Fe_3O_4, see Glazyrin *et al.* [11] for studies to ~25 GPa and Xu *et al.* [12] for investigations to higher pressures exceeding 50 GPa, and references cited in those publications. Strong onsite repulsion effects associated with the partially filled narrow 3d band render insulating behavior to mixed-valence magnetite $Fe^{3+}(Fe^{2+}Fe^{3+})O_4$ at ambient pressure. These strong electron correlation effects and nonmetallic behavior seem to persist to very high pressures exceeding ~50 GPa [13]. Beyond this pressure, only annealing at high temperatures of 1050 K [14], or pressurizing to much higher pressures of ~120 GPa at room temperature (RT) yields a positive temperature coefficient of resistance and resistivity values typical of a poor metal in the vicinity of RT [12]. There is controversy about magnetic-electronic aspects of the compound in the low-pressure regime where there are claims and counterclaims for an electronic change from x-ray magnetic circular dichroism and ^{57}Fe Mössbauer spectroscopy (MS) investigations, respectively [11,15].

Here, we conduct a similar comparative investigation of the other end member $Fe^{2+}(Fe^{2+}Ti^{4+})O_4$. By using

---

[*] Author to whom all correspondence should be addressed: xuw@post.tau.ac.il

a combination of variable cryogenic temperatures ^{57}Fe MS and electrical-transport (resistance) probes as well as complementary x-ray diffraction (XRD) structural studies at *in situ* pressures to ∼90 GPa, we provide insight into the interplay between the magnetic-electronic aspects and lattice-structural responses at varying degrees of high densities.

It is also anticipated that this will serve as important reference information when interpolating to members of the solid-solution series of pertinence to rock magnetism and the geosciences. In addition, spinels represent an abundant structure type in both the lower crust and the upper mantle. They are known to exhibit a pressure-induced phase transformation to orthorhombic post-spinel $CaFe_2O_4$-, $CaMn_2O_4$-, and $CaTi_2O_4$-type structures; for a review, see the reference of Errandonea [16]. There are hardly any magnetic-electronic investigations of these post-spinel phases in comparison to the extensive structural investigations already published [16].

Previous high-pressure XRD structural studies have demonstrated that Fe_2TiO_4 undergoes a series of structural phase transitions from cubic ($Fd\bar{3}m$) to tetragonal ($I4_1/amd$) at ∼9 GPa, and then to an orthorhombic post-spinel structure ($Cmcm$) at ∼16 GPa [1,17]. The tetrahedral sites of the spinel evolve to eightfold coordinated sites in the post-spinel structure [18], in addition to structurally adjusted sixfold coordinated sites occurring in which the Fe/Ti remains chemically disordered. Yamanaka *et al.* [1,17] have also shown that, in a number of $Fe_{3-x}Ti_xO_4$ compositions, the transition pressure to an orthorhombic post-spinel phase has a nearly linear dependence on x at RT. It varies from 25 GPa for $x = 0$ (magnetite) to ∼16 GPa for $x = 1$ in the other end member, ulvöspinel. In particular, in Fe_2TiO_4, another high-pressure polymorph was deduced to occur above 50 GPa. Refinements of XRD data in the range 50–60 GPa in terms of $Pmma$ symmetry, corresponding to Fe/Ti chemical order in sixfold coordinated sites, yield the highest reliability factors [17]. This represents a nonisomorphic subgroup of the $Cmcm$ SG. Later Raman pressure studies to ∼57 GPa [19] seem to corroborate this sequence of structural transitions. Yamanaka *et al.* [17] also present Fe $K\beta$ x-ray emission spectroscopy (XES) results for Fe_2TiO_4. They contend therein that spin crossover to diamagnetic low-spin (LS) Fe initiates as low as ∼14 GPa at RT and progresses to completion by ∼30 GPa. This would have important geomagnetic implications given the role of the Fe_3O_4-Fe_2TiO_4 solid solution series in this regard. The XES experiments do not reveal a detailed picture of the crystal-chemistry changes associated with the purported spin crossover and its relation to the structural transitions mentioned above. For example, does the spin pairing occur at all of the sixfold coordinated Fe sites? A much more suitable probe of this detail is obtained by variable temperature ^{57}Fe MS, which is a direct probe of the Fe magnetic-electronic state even under *in situ* extreme pressure-temperature conditions. In this regard, exceedingly important and unique information may be discerned, in that spin and oxidation states and their distribution and abundances in the lattice structure are obtained from the deconvolution of subcomponents in a spectrum [20]. We implement this to ∼90 GPa, well beyond previous high-pressure MS studies on ulvöspinel by Wu *et al.* [21] limited to 24 GPa at RT. In addition, we extend the XRD measurements and analysis to ∼90 GPa, also to well beyond the previous investigations of Yamanaka *et al.* [1,22]. Our complementary electrical resistance measurements complete the picture of the pressure evolution of strong electron correlations in the various structural phases.

II. EXPERIMENTAL

The Fe_2TiO_4 sample is the same as that used in the previous study by Wu *et al.* [21]. This involved a solid-state reaction of stoichiometric quantities of Fe_2O_3 and TiO_2 at a predetermined oxygen fugacity using an appropriate CO-CO_2 mixture. The Fe_2O_3 precursor material was enriched to ∼63% ^{57}Fe by thorough mixing of near fully enriched and natural abundance oxides. The cubic structure and magnetic properties were compatible with previous reports of phase pure samples at ambient pressure [1,2], as confirmed by conventional powder XRD and also by variable cryogenic temperature MS in our laboratory.

^{57}Fe Mössbauer-effect studies were carried out using a ^{57}Co(Rh) 10-mCi point source in the 5–300 K temperature range involving a top-loading liquid-helium cryostat [23]. The typical collection time of a spectrum was ∼24 h. Spectra at the highest pressures near ∼90 GPa at variable cryogenic temperatures, involving much shorter data collection times, were recorded at the European Synchrotron Radiation Facility (ESRF, Grenoble, France) using synchrotron Mössbauer source methodology [24]. Spectra were analyzed using appropriate fitting programs from which the hyperfine interaction (HI) parameters and the corresponding relative abundances of the spectral components were derived [25,26]. The isomer shift (IS) in this paper is calibrated relative to an α-Fe foil at ambient conditions. The Tel-Aviv University (TAU) miniature piston-cylinder DAC was used [27], with anvils having 300 μm diameter culets for pressures to ∼60 GPa and 200 μm diameter culets for $P > 60$ GPa. Samples were loaded into 100 to 150 μm diameter cavities drilled in a rhenium gasket for MS studies. This also served as an effective collimator for the 14.4 keV γ rays. Liquid argon was used as a pressurizing medium [28,29]. A few ruby chips were included in the sample cavity for pressure measurements by way of the ruby $R1$ fluorescence pressure marker.

Powder XRD measurements were carried out at RT in angle-dispersive mode with a wavelength of $\lambda = 0.3738$ Å at the Pression Structure Imagerie par Contraste à Haute Énergie (PSICHÉ) beamline of Synchrotron SOLEIL (Paris). Pressurization was by means of a TAU piston-cylinder DAC with anvils having 200 μm diameter culets. The sample with a few ruby chips was loaded into a 100 μm diameter cavity drilled in a rhenium gasket preindented down to a final thickness of ∼15 μm, and Ne or He was used as the pressure transmitting medium. Diffraction images were collected using a MAR345 image plate detector and integrated using the FIT2D [30,31] and DIOPTAS software [32]. Powder diffraction patterns were analyzed using the GSAS-II software [33] to extract the unit-cell parameters.

The intensities of the diffraction peaks are affected by instrumental and grain-size issues (diamond x-ray absorption and low statistics in random distribution of the sample crystallites). Therefore, the Rietveld refinement of the powder diffraction patterns did not result in a good enough fit. Hence, diffraction patterns were analyzed by using the whole profile fitting (Pawley) method [34]. Diffraction spectra mainly exhibit peaks from the Fe_2TiO_4 sample, as well as minor peak contributions from the gasket (Re) and the pressure medium (Ne). These phases were considered in the refinements. The reliability factor R_{wp} obtained in the refinement of each of the powder diffraction patterns is $\sim$1%.

Resistance measurements in the TAU piston-cylinder DAC involved samples loaded into $\sim$100 μm cavities drilled in rhenium gaskets insulated with a layer of Al_2O_3-NaCl (3:1 wt. %) mixed with epoxy. Conductive epoxy was used to connect exterior conducting Cu wires to microscopic triangular cut Pt foils. The latter served as electrodes in a direct current (DC) four-probe configuration, leading from the pavilion of the anvil to near the center of the culet so as to overlap with the sample upon closure of the DAC. Six of such electrodes were configured on the culet to permit measurements in various four-probe arrangements at a given pressure. This built-in redundancy affords a means of checking the effects of any pressure distribution in the regions between the leads and provides alternatives in case of any lead breakages in the compression sequence. A few ruby fragments for pressure determination were located in the region between the Pt electrode tips overlapping the sample. No pressure transmitting medium was used, but pressure is effectively transmitted to the sample upon compression by way of the surrounding insulation. Pressure gradients are expected to be small in the distances (20–30 μm) between the tips of the Pt electrodes across which voltage measurements are made. For variable low-temperature measurements, the DAC was placed on a probe connected to a dipstick stepper-motor assembly, which by computer control slowly changed the height of the DAC above the cryogen level in a liquid nitrogen or helium Dewar. The temperature was monitored by a Lakeshore Si (DT-421-HR) diode in proximity to the DAC.

The calibration scales mentioned in Ref. [35] were used for pressure determination from the ruby fluorescence measurements. The error in the pressure determination is 5–10% of the reported average pressure from the ruby fluorescence measurements in the case of the MS and resistance experiments. In the case of the XRD measurements, pressure was determined from the ruby fluorescence spectra up to $\sim$51 GPa. The Ne equation of state (EOS) was used to ascertain pressures in the range 10–85 GPa [36]. Both methods give rather similar pressure values, the difference not exceeding 0.5 GPa. The error in the pressure determination is about 2% of the reported average pressure.

III. RESULTS AND DISCUSSION

The magnetic-electronic behavior up to $\sim$90 GPa is summarized in the evolution of representative Mössbauer spectra at RT and lowest cryogenic temperatures (LTs) in Fig. 1.

In fitting the Mössbauer spectra in this range, we first consider the spectrum and analysis of the spinel $Fe^{2+}(Fe^{2+}Ti^{4+})O_4$ at ambient pressure. Fe/Ti is disordered on the octahedral *B* sites, and this leads to a distribution of Fe local environments (next nearest neighbor variations). The tetrahedral *A* sites share some corners with the *B* sites, and therefore, the associated tetrahedral Fe also experiences a distribution of next nearest neighbor environments. Therefore,

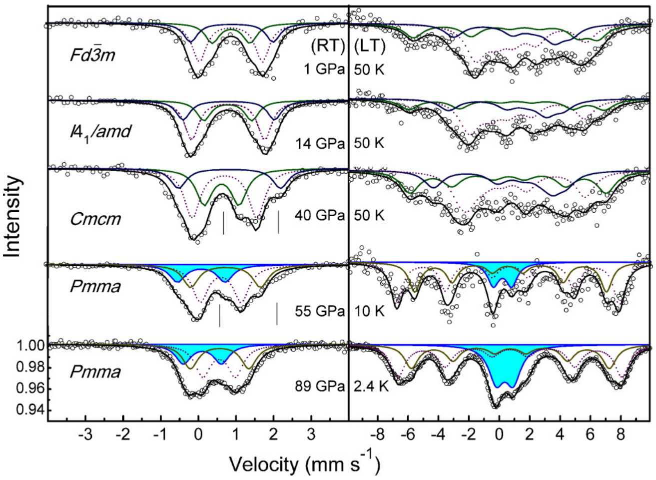

FIG. 1. Representative Fe Mössbauer spectra at RT (left panel) and LTs (right panel), in the pressure regimes discussed in the text. Solid lines through the data points represent the overall fit to the data from the sum of subcomponents shown. Dotted line subcomponents refer to the four- or eightfold coordinated sites, and other subcomponents refer to sixfold coordinated sites, discussed in the text. The vertical lines are a guide to the eye as to where changes occur in the spectral profile compared to the preceding pressure regime. The shaded component in the *Pmma* phase represents LS Fe sites.

the HI parameters most directly affected by the local lattice environment and the atomic disorder, quadrupole splitting/shift (QS) and magnetic hyperfine field H_{hf} will have a distribution of values [25]. The spectrum at RT has a broadened doublet profile with poorly resolved shoulder features in the inner parts. This hints at two strongly overlapping QS contributions from the *A* and *B* sites which are not well resolved. This has been rationalized from the orbital level scheme and how the degeneracies are lifted due to the distortions at the *A* and *B* sites. The minority spin (↓) occupation of the lowest-lying $3d$ orbital levels has the most significant effect on the resultant electric field gradient (EFG) and consequently determines the QS [37]. This similar occupation of the lowest-lying $3d$ orbital singlet for *A* and *B* sites leads to comparable QS values and hence the strong overlap of components from these sites [38,39]. Moreover, there is a distribution of QS values from the Fe/Ti disorder effects which is expected to result in multiple *B*-site local environments and consequentially multiple *A*-site local environments as well. All of this may be manifested as appreciable line broadening of discrete subspectra fitted to the spectral profile. Similar unresolved features occur in the complex magnetic spectra at $T \ll T_N$, attributable to both a distribution of H_{hf} values from the varied magnetic superexchange contributions as well as a QS distribution associated with disorder at *B* sites. Because of the strong overlap of *A*- and *B*-site contributions, it is difficult to determine what the true distributions are for the QS and H_{hf} parameters. Nakamura and Fuwa [2] have rather used a combination of two broadened Lorentzian subspectra to represent the distributions associated with the *A* sites and similarly associate two components with the *B* sites. This four-component fitting is the minimum number of Lorentzian profiles required to render a good fit to the overall spectral envelope, over an extended temperature range 300–16 K. In each case of both *A* and *B* sites, the two broadened components are supposed to represent two different degrees of partial order in the unit cells, and not a completely random arrangement of Fe/Ti on the *B* sublattice [2].

We have adopted a similar minimal number of broadened discrete subcomponents model to analyze our temperature dependent spectra measured at high pressure. Spectra taken at high pressure in the DAC also have extrinsic sources of broadening from the customized point source [23], as well as from pressure gradients and the associated stress distribution in the pressurized cavity. So the true distributions associated with the HI parameters would be even more difficult to determine unambiguously. The IS, QS, and H_{hf} values derived from the fitting with broadened Lorentzian components then represent the averages of the associated parameter distributions and are quite insensitive to the degree of line broadening (be it intrinsic or from extrinsic effects [40]). This is expected to ensure reliable qualitative interpretation of the data. As a check, selected spectra fitted with the full transmission integral yielded similar HI parameters and relative abundances of subcomponents to that obtained in fitting with Lorentzian profiles.

Hyperfine interaction parameters are constrained, or starting values chosen, to ensure consistency between RT and LT analyses. Linewidth broadening is permitted to artificially account for the local environment distribution and thickness effects from the isotopic enrichment [40]. The pressure evolution of these parameters is depicted in Fig. 2, as derived from typical fits shown in Fig. 1. Three pressure regimes are delineated, partly based on previous structural data of Yamanaka *et al.* [1,17], and these are discussed in detail in the following subsections. The results and analysis of Mössbauer data are correlated to the pressure dependences of our XRD structural data in Figs. 3 and 4, as well as resistance data (Fig. 5) in these regimes.

A. Cubic and tetragonal phases, ambient pressure to ∼16 GPa

X-ray investigations from ambient pressure to 8 GPa show the structure to be cubic spinel at RT. From thereon up to 16 GPa, it is tetragonally distorted [1].

Figure 1 shows RT and LT Mössbauer spectra at 1 and 14 GPa representative of this low-pressure regime. The profiles of the spectra at RT have narrowed and become more symmetrical compared to the spectrum at ambient pressure. Using the linewidth (0.4 mm s^{-1}) fitted at ambient pressure, the RT spectra above 1 GPa could be satisfactorily fitted with three quadrupole doublets with an intensity ratio 1:0.5:0.5, supposed to represent high-spin (HS) Fe in the *A* sites [HS(IV)] and two categories of *B* sites [HS(VI-1), HS(VI-2)], respectively. This provided the best fit to both LT and RT spectra and is a slight variant on the four-component model of ambient pressure, in that the two suites representing tetrahedral *A* sites are now merged, whereas the two suites associated with the octahedral *B* sites are retained. This change is a result of the sharpening of the spectrum. The change occurs mainly with the *A*-site QS components, likely because these also have contributions from the dynamical Jahn-Teller effect in the cubic structural phase.

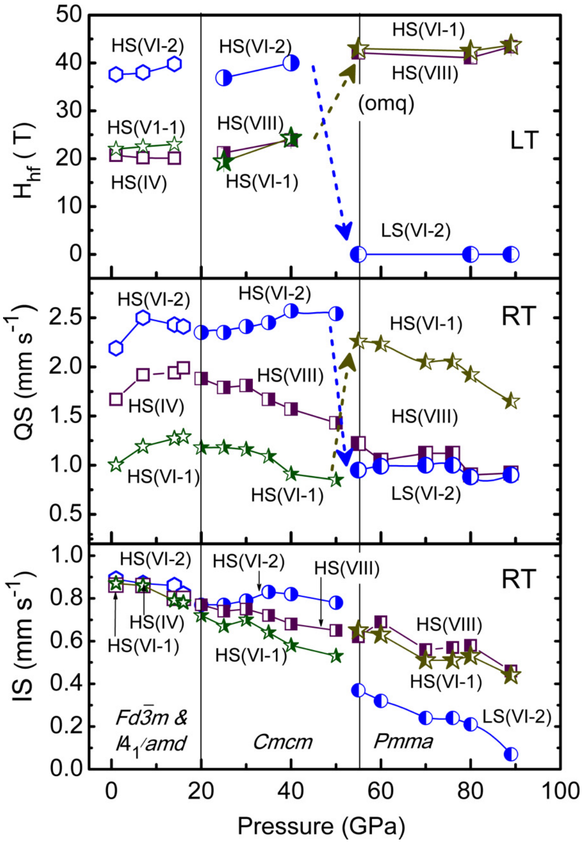

FIG. 2. Pressure dependences of the HI parameters from best fits to the Mössbauer spectra. Vertical error bars do not exceed twice the size of the symbols but are omitted to avoid clutter in the plots. Top panel has saturation magnetic hyperfine field H_{hf} values from the LT spectra. QS and IS parameters from spectra at RT are in the middle and bottom panels. Three pressure regimes demarcated by the vertical lines have been identified and discussed in the text. Roman numerals IV, VI, and VIII refer to four-, six-, and eightfold coordinated tetrahedral, octahedral, and bicapped trigonal prismatic sites, respectively. Spectra in the ambient to 20 GPa range, where XRD discerns cubic and then tetragonal behavior at 300 K, are best fit at this temperature with three QS components having similar IS values as discussed in the text. These are associated with two categories of sixfold coordinated Fe sites, HS(VI-1) and HS(VI-2), and fourfold coordinated sites HS(IV). Spectra in the regime 20–50 GPa are deconvoluted in a similar way. The structural transformation of four- to eightfold coordinated HS(VIII) sites and evolution of the sixfold coordinated sites across the $I4_1/amd \rightarrow Cmcm$ reconstructive transition are described in Ref. [18]. Spectral analysis suggests two categories of large QS [HS(VI-2)] and small QS [HS(VI-1)] persist into this regime. Large H_{hf} values associated with orbital moment quenching are indicated by the (omq) label. Parameters for the LS sites are delineated by the LS(VI-2) labels.

These are probably very sensitive to pressurization, similar to the sensitivity seen in varying the temperature [20]. A plot of the pressure dependence of the HI parameters is depicted in Fig. 2.

The three components have the same IS (centroid) but different QS values. The component with largest QS ∼ 2.5 mm s^{-1} has a large average field value of H_{hf} ∼ 40 T from its saturation magnetization at 50 K. We attribute this

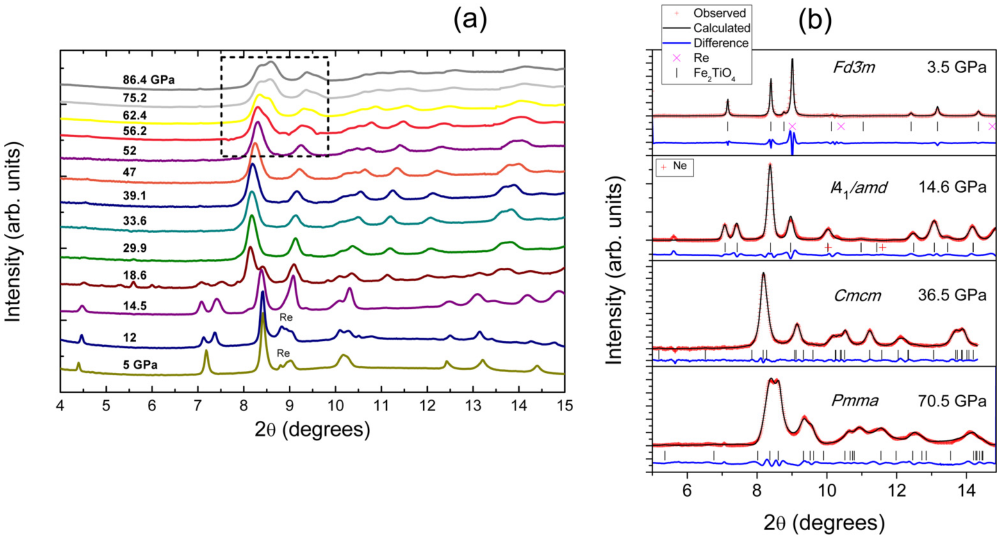

FIG. 3. (a) Pressure evolution of the XRD patterns up to ∼86 GPa ($\lambda = 0.3738$ Å). Contamination reflections from the rhenium gasket are indicated. The dashed box highlights where changes in reflection profiles occur at very high pressure, supposed to be an indicator of a $Cmcm \rightarrow Pmma$ symmetry lowering due to a Fe/Ti disorder → order transition at sixfold coordinated sites, as discussed in the text. (b) Examples of refinements of the XRD patterns at pressure in the various structural phases.

to one category of sixfold coordinated (octahedral) sites, designated HS(VI-2). The other two subspectra have low average field values $H_{hf} \sim 20$ T but with different QS values of 1 and 1.5 mm s^{-1}, attributed to a second category of octahedral sites designated HS(VI-1) and to the tetrahedral sites designated HS(IV), respectively. It should be noted that the quoted H_{hf} values must be interpreted as average values of the true distributions which are represented here by broadened Lorentzian profiles. In these magnetic spectra at LT, the overall spectral profile dictates that both B sites have negative QS values, and the A site has a positive QS, as explained in Ref. [2].

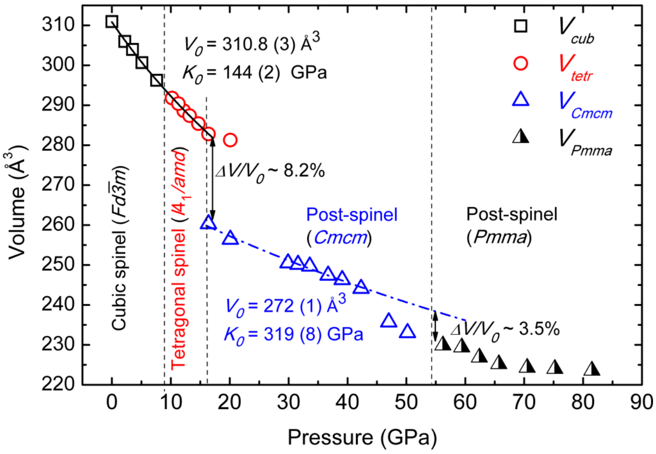

FIG. 4. Pressure dependences of the unit-cell volume normalized to the number of formula units therein, of the various structural phases. The vertical error bars do not exceed the size of the symbols. Solid lines through the data symbols are fits with a Birch-Murnaghan EOS to obtain bulk modulus K_0 and constraining its derivative at $K'_0 = 4$ [53]. The vertical dashed lines demarcate the pressures where structural transitions are onset.

It may also be noted in Fig. 2 that, from 1 to ∼8 GPa in the cubic phase at RT, the QS of the sites have a much stronger pressure dependence than when the compound becomes tetragonal as pressure rises above 8 GPa. This is another indicator of the sensitivity of dynamical Jahn-Teller distortions

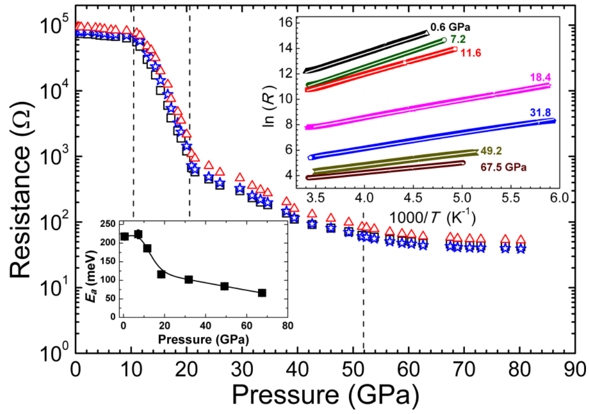

FIG. 5. Pressure dependence of the resistance at 300 K in the main panel. Different symbols refer to various four-probe arrangements and interelectrode distances, based on selections from the six electrodes configured in the sample cavity. The pressure dependences are the same in all three cases, as a check of any effects of pressure distribution or electrode-sample contact issues. Top right inset shows linearized temperature-dependent data at various pressures assuming Arrhenius activated hopping transport, $\ln(R) \propto \frac{E_a}{k_B T} +$ const. The activation energy E_a is obtained from the slope of fits to these plots, from whence the charge gap for intrinsic conduction $E_g = 2E_a$ is derived. Bottom left-hand inset shows the pressure dependence of E_a; the solid line through the data points is to guide the eye. Dashed vertical lines in the main panel delineate onset pressures to new structural phases deduced from appreciable changes in pressure dependences of R(300 K) and E_a for comparison with XRD experiments, see text and preceding Fig. 4.

and its associated QS contribution to applied pressure and stresses in the sample, as mentioned earlier. This also marks a boundary where the cubic-to-tetragonal transition temperature has risen from $T_{J\text{-}T} \sim 163$ K at ambient pressure up to RT by ~ 8 GPa.

As in the interpretation of spectra at ambient pressure, the two categories of HS(VI) octahedral sites in this pressure regime are ascribed to two levels of partial Fe/Ti order in the B sublattice [2]. In Fig. 2, the large field $H_{hf} \sim 40$ T of HS(VI-2) is comparable to the spin-only value obtained from the Fermi contact interaction term $H_C = +(\text{const.})\mu_B[\rho_s^{\uparrow}(0) - \rho_s^{\downarrow}(0)]$ involving the net spin-up and spin-down s-electron density at the nucleus. The $H_{hf} \sim 20$ T values of HS(IV) and HS(VI-1) components are much smaller than typical ferrous values of $H_C \sim 44$ T. This is suggestive of an opposing unquenched orbital moment term $H_L = -2\mu_B\langle r^{-3}\rangle\langle l_Z\rangle$ contributing to $H_{hf} = H_C + H_L$ at these sites [41–43]. According to Nakamura and Fuwa [2], these are also sites where the partial Fe/Ti order in the unit cells of the B sublattice is distinct from that of HS(VI-2).

X-ray pressure results of our sample are consistent with that of Yamanaka *et al.* [1]. Diffraction patterns at RT in the range 8–16 GPa may be refined in terms of a tetragonal phase (SG $I4/amd$), see Figs. 3 and 4. As the tetragonal phase emerges at 8 GPa, the weak monotonic decrease of the resistance at RT in the cubic phase changes to a much stronger negative pressure dependence as the tetragonal phase is pressurized, see Fig. 5. This results in a decrease in resistance by more than two orders of magnitude in the range 8–20 GPa, after which there is a change back to a much weaker pressure dependence again for $P > 20$ GPa. The data are well represented by activated transport processes $R = R_0\exp[E_a/(k_BT)]$, where E_a is the activation energy, as seen by the linearized data sets $\ln(R)$ vs $1/T$ in the inset of Fig. 5. The changes in E_a values in the inset mirror the appreciable changes in pressure dependences of the $R(300\text{ K})$ data in the main panel. We consider this corroboration of the ~ 8 and ~ 16 GPa phase transition boundaries identified in the XRD data. Any difference in transition pressures identified by the two techniques is attributed to the degree of hydrostaticity from the pressure transmitting medium used in the pressurized cavity, see experimental Sec. II.

B. *Cmcm* post-spinel phase in the range 20–55 GPa, initiation of site-specific spin crossover and orbital moment quenching

The emergence of a new structural phase beyond 16 GPa is associated with a substantial decrease in unit-cell volume, see Fig. 4. The x-ray diffraction results of Yamanaka *et al.* [17] and our data and analysis in Figs. 3 and 4, show that, above ~ 20 GPa, Fe_2TiO_4 transitions to the orthorhombic post-spinel $CaTi_2O_4$-type structure with SG *Cmcm*. There is also a change to a much lower compressibility with a substantial increase in bulk modulus from $K_0 \sim 144$ to 319 GPa.

In this post-spinel structure, Fe^{2+} occupies so-called M1 (eightfold coordinated) sites, and Fe^{2+} and Ti^{4+} occupy M2 (sixfold coordinated) sites with occupancy ratio 1:1:1 [17], see Fig. 6. In this pressure regime, the spectral envelope of Mössbauer data at RT become broader and more asymmetrical, yet the low-temperature spectra remain somewhat similar to the spinel phase in that both large and low average H_{hf} distributions can be fitted, Fig 1, arising from the Fe/Ti partial order proposed in the sixfold coordinated sites [2]. The Mössbauer spectra at RT are best fit with three components as in the spinel phase, namely one M1 [designated HS(VIII)] and two M2 sites, designated HS(VI-1) and HS(VI-2), conforming to a ratio of 1:0.5:0.5 for HS(VIII) : HS(VI-1) : HS(VI-2). Hyperfine interaction parameter values are plotted in Fig. 2. The two quadrupole doublets for the M2 sites indicate that these are distinct categories of sixfold coordinated sites with different local environments, and HS(VI-1) involves less site asymmetry than HS(VI-2), based on the QS values [37]. Here, HS(VI-1) and HS(VIII) have relatively small average field $H_{hf} \sim 20$ T values at low temperatures, indicative of an unquenched orbital contribution, also discussed in Sec. III A.

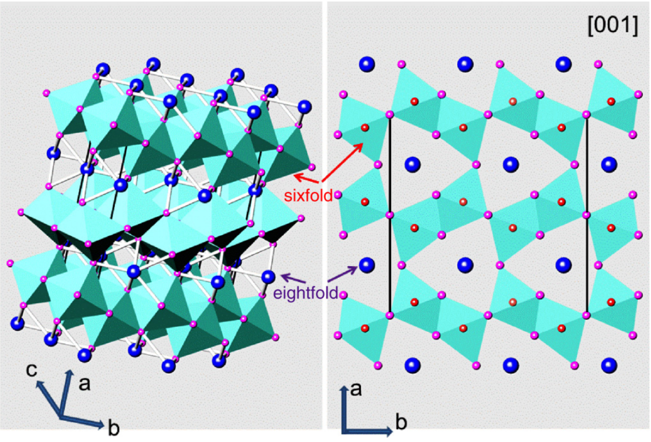

FIG. 6. High-pressure structure of Fe_2TiO_4 post-spinel with SG *Cmcm*. Locations of six- and eightfold coordinated sites are indicated. Fe and Ti are disordered on the sixfold coordinated sites. The left panel is a perspective view and right panel shows the projection down the c axis and characteristic bidirectional herring bone arrangement.

In spite of the large volume change $\Delta V/V_0 \sim 8\%$ at the tetragonal-spinel/post-spinel structural transition, the IS does not show an associated discontinuous decrease expected upon densification [44]. This is because the spinel sites undergo compensating changes to higher coordination HS(IV) → HS(VIII), which is expected to increase IS. The IS of the three components separate out in this pressure range as well, due to the different compressibilities of the M1 and M2 polyhedrons. Fe^{2+} in the HS(VI-1)-designated site is apparently in a more compacted sixfold coordinated local environment than HS(VI-2), inferred from its lower IS value. A further inference from the pressure dependences of the IS and QS parameters in Fig. 2 is that one category of octahedral sites HS(VI-2) with slightly increasing QS undergoes further distortion while the other sites HS(VIII) and HS(VI-1) become less distorted. These further pressure-instigated distortions to HS(VI-2) will increase the crystal field (CF) splitting, with implications for spin crossover if a large enough CF splitting is attained [45,46]. Here, HS(VI-1) and HS(VIII) have monotonically decreasing QS values, perhaps indicating progressively decreasing polyhedral distortions as a cooperative lattice compensation for the behavior of HS(VI-2).

Therefore, according to the MS data up to ∼50 GPa, three categories of sites have Fe^{2+} parameters typical of the HS state, see Fig. 2 [47]. The LT spectra also show no evidence of a diamagnetic central QS doublet anticipated for LS Fe^{2+} (atomic spin $S = 0$). This contradicts the claims from XES experiments that spin crossover to a LS state is initiated as low as ∼14 GPa [17]. Those experiments, limited to ∼31 GPa, involve monitoring small intensity changes of relatively weak $K\beta'$ satellite features ascribed to the HS abundance and may be prone to systematic errors.

In our XRD data in the range 40–52 GPa, the shift of the most intense diffraction peak near $2\theta \sim 8^\circ$ develops an appreciable increase in positive pressure dependence, see Fig. 3(a). The refinements also show that the associated unit-cell volume of the *Cmcm* structure starts to deviate from the EOS of the HS post-spinel phase in this pressure range, see Fig. 4.

At pressures exceeding ∼50 GPa, changes are discerned in the RT and LT MS spectra compared to lower pressures. These changes are highlighted by vertical bars in the RT spectra at 55 GPa depicted in Fig. 1. In the associated LT spectrum, the smeared features in the central region at lower pressures now become more structured. When considering the profiles of the RT and LT Mössbauer spectra, we are still able to fit each of these with a minimum of three subcomponents, see Fig. 1. The spectral analysis shows that two categories of highly and less distorted sixfold coordinated sites prevail. The spectral component associated with eightfold coordinated sites has similar HI parameters to that of the preceding pressures below ∼50 GPa. This is adequately modeled by a single broadened quadrupole doublet with QS ∼ 1.5 mm s^{-1}. However, the additional two doublets representing Fe in sixfold coordination show starkly different temperature dependences. One of the remaining doublets with much larger QS ∼ 2.3 mm s^{-1} and IS ∼ 0.7 mm s^{-1} at RT and 55 GPa does show a magnetic splitting at LT, but with a much bigger $H_{hf} \sim 42$ T compared to the preceding pressures of this *Cmcm* post-spinel regime. The other doublet with smaller QS ∼ 1 mm s^{-1} and IS ∼ 0.4 mm s^{-1} values at RT and 55 GPa does not exhibit a magnetic splitting ($H_{hf} = 0$ T) down to liquid helium temperatures and gives rise to intensity in a narrow region near zero velocity. This together with the evolution of large $H_{hf} \sim 42$ T magnetic splittings for the other components accounts for the development of more structured features in the central regions of the spectra.

Figure 5 also shows that the pressure dependence of the resistance at RT starts to decrease as the sample is compressed beyond ∼40 GPa to a plateau at $P > 70$ GPa.

Thus, the combination of changes in magnetic behavior seen in the (LT) magnetic Mössbauer spectra, pressure dependence of unit-cell volume, and R(300 K) behavior onset in the vicinity of ∼50 GPa marks this as an electronic transition region.

The evolution of HI parameters across this phase transition region at ∼50 GPa, Fig. 2, is thus interpreted in the following way: HS(VI-2) with large QS ∼ 2.5 mm s^{-1} and IS ∼ 0.8 mm s^{-1} at RT transitions to the component with much smaller QS ∼ 1 mm s^{-1} and IS ∼ 0.4 mm s^{-1} values and is diamagnetic. These are the telltale signatures of a HS → LS transition [47]. The spin pairing accounts for the change to a relatively small QS value and the diamagnetism (atomic spin $S = 0$) from the orbital population redistribution in t_{2g}- and e_g-derived sub-bands, $t_{2g}{}^4 e_g{}^2(\uparrow\downarrow\uparrow\uparrow)(\uparrow\uparrow) \rightarrow t_{2g}{}^6 e_g{}^0(\uparrow\downarrow\uparrow\downarrow\uparrow\downarrow)$ (), see Fig. 7. As HS(VI-2) only constitutes ∼25% of sixfold coordinated Fe sites, the spin crossover in Fe_2TiO_4 only entails partial conversion of Fe sites to the LS state, namely those octahedral locations with sufficiently large site asymmetry corresponding to QS ∼ 2.5 mm s^{-1} in the HS state.

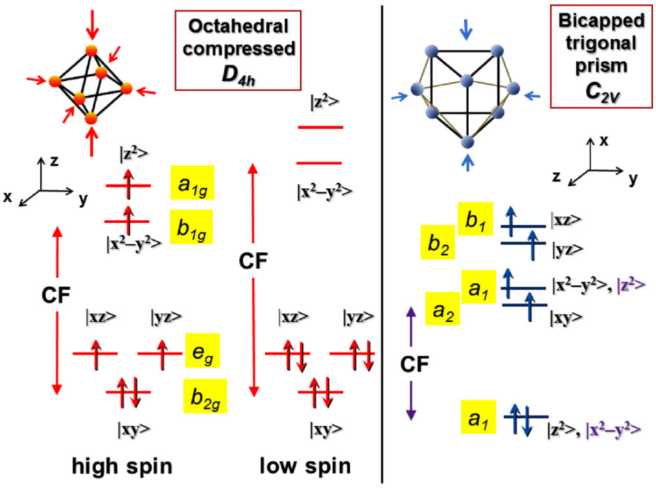

FIG. 7. Schematic of CF split 3d electronic level scheme for Fe^{2+} involving tetragonal distortions in octahedral (sixfold) coordination and compression of bicapped trigonal prism (eightfold coordination site), the latter is adapted from Burdett *et al.* [54]. Irreducible representation symmetry labels for the orbitals are indicated in the yellow blocks.

The $V(P)$ data of Fig. 4 exhibits a deviation from the HS *Cmcm* EOS onset in the range 40–45 GPa, leading to a unit-cell volume change of $\Delta V/V_0 \sim 3.5\%$. This relatively small unit-cell volume change is considered corroboration that spin crossover is limited to a fraction of sites in the unit-cell, similar to what has been discerned in ferropericlase $Mg_{1-x}Fe_xO$ (for $x \leqslant 0.39$) [48]. The experimentally determined volume change is also compatible with an estimate obtained from considering the ∼21% relative difference in octahedral volume $V_{\text{oct}} \propto (r_{\text{Fe}} + r_{\text{O}})^3$ expected for HS and LS FeO_6 polyhedrons, where the radii in brackets are those of Fe and O nearest neighbor atoms [49,50], and noting that spin crossover is limited to highly distorted octahedra (VI-2) constituting one quarter of the Fe sites (i.e., one sixth of all cations, [17]) in the structure.

Differences in onset pressures of LS signatures ascertained from MS, XRD, and resistance data are attributable to different pressure transmitting media used and consequently how different degrees of hydrostaticity affect spin crossover [51].

This partial spin crossover has an associated cooperative lattice response. Less distorted HS(V1-1) sites with relatively small QS ∼ 1 mm s^{-1} values in the *Cmcm* phase at lower pressure now take on larger QS ∼ 2.3 mm s^{-1} values indicative of an increase in site asymmetry [37], linked to the spin transition at the other VI-2 sites. The QS of HS(VI-1) does not exceed the critical QS value of ∼2.5 mm s^{-1}, which was attained in HS(VI-2) and which signified sufficient octahedral distortion and an associated increase in CF to trigger the spin crossover at VI-2 sites.

Now consider the magnetic behavior deduced from fitting the LT spectra, see Fig. 1. The small $H_{hf} \sim 20$ T values of HS(VIII) and HS(VI-1) of the *Cmcm* regime give the smeared features in the centralized region of the magnetic spectrum, e.g., see LT spectrum at 40 GPa in Fig. 1. Above ~50 GPa, these smeared contributions evolve to much sharper features, indicative of increased separation of the lines of each sextet spectral component due to a substantial increase in magnetic hyperfine splitting $H_{hf} \sim 42$ T. This is close to the spin-only value contribution to the magnetic moment of Fe^{2+} and its Fermi contact term contribution $H_C \sim 44$ T. This signifies that the orbital moment term H_L opposing H_C has quenched at HS(VIII) and HS(VI-1) sites, recalling that $H_{hf} \sim H_C + H_L$. This is rationalized as follows.

At the onset of spin crossover at HS(VI-2) sites, the cooperative lattice response of HS(VIII) and HS(VI-1) polyhedra is such that the b_{2g} and a_1 lowest-lying orbital levels are shifted to sufficiently below higher-lying levels (e_g and a_2, respectively) in Fig. 7, for orbital quenching to occur. The minority spin electron (↓) then predominantly populates these lowest-lying orbitals which do not render an orbital moment contribution [43]. Furthermore, the maximum value of the EFG, V_{zz}, and thus QS [37] depends primarily on the 3d orbital occupancy of the minority spin electron. This is because $V_{zz} \propto e(2n_{xy} - n_{yz} - n_{xz} - 2n_{z^2} + 2n_{x^2-y^2})/\langle r^3\rangle$, where $n_{xy}, n_{yz}, \ldots$ denote the occupancy of the minority spin in orbitals $|xy\rangle, |yz\rangle, \ldots$, respectively [38,52]. The change in polyhedral distortion at both HS(VI-1) and HS(VIII), in response to the spin state change at HS(VI-2) and associated lattice response, is such that changes in low-lying 3d level spacing in Fig. 7 lead to a change in orbital occupancy. Consequentially, both the orbital moment quenches and V_{zz} changes to result in the new appreciably bigger QS value of ~2.3 mm s^{-1} for HS(VI-1). Note this is below the "critical" value of ~2.5 mm s^{-1} which triggered spin crossover in HS(VI-2) in the *Cmcm* phase. Whereas in eightfold coordinated HS(VIII) sites with a completely different level scheme to sixfold coordinated sites (see Fig. 7), this change in orbital occupancy has much less impact on V_{zz} than in sixfold coordinated sites, but still leads to orbital moment quenching [43].

C. 55–90 GPa, persistent partial spin crossover and *Pmma* post-spinel phase

When considering the profiles of the RT and LT Mössbauer spectra upon further compression beyond ~55 GPa, we are still able to fit each of these with a minimum of three subcomponents, see Fig. 1. The analysis of the MS spectra show the abundances of the three components are in the ratio 1:0.5:0.5. The component representing Fe in eightfold coordinated sites being of equal abundance to the combination of the other two sixfold coordinated sites. The IS and QS parameters of the components have monotonically decreasing values upon further compression steps to ~90 GPa. The partial spin conversion initiated in the *Cmcm* phase remains limited to a fraction of the Fe sites up to the highest pressure of ~90 GPa attained in this paper. This is exemplified in the magnetic spectrum at the highest pressure of ~89 GPa in Fig. 1. A doublet of ~25% abundance occurs in a narrow region near zero velocity corresponding to the diamagnetic LS species. The remainder of HS(VI-1) and HS(VIII) sites continue to both have a magnetic ground state involving a quenched orbital moment and associated $H_{hf} \sim 42$ T.

Yamanaka *et al.* [17] contend from x-ray pressure studies that a further structural adjustment occurs in the vicinity of ~50 GPa. They have refined the patterns above ~50 GPa in terms of the *Pmma* SG, a nonisomorphic subgroup of *Cmcm*. Yamanaka *et al.* only show two data points for such *Pmma* refinements in the range 50–60 GPa. It may be noted that, in our XRD data, extended to much higher pressures of 86 GPa, conspicuous splittings occur in some of the reflections in the range 52–56 GPa indicative of some symmetry lowering, see Fig. 3. In accord with Yamanaka *et al.* [17], we have chosen to refine the patterns above ~50 GPa in terms of the symmetry-lowering subgroup *Pmma* of *Cmcm*. A slightly new trend in the pressure dependence of the volume is then followed up to at least 80 GPa, see Fig. 4. Yamanaka *et al.* have attributed this structural adjustment to atomic ordering of Fe/Ti in the sixfold coordinated sites. Within this post-spinel variant, two distinct Fe sites (sets of bond lengths) occur in both eightfold and sixfold coordination environments.

Recall that spin-state changes at specific octahedral sites (VI-2) are onset within the post-spinel *Cmcm* structure preceding this transition to the *Pmma* phase. We speculate that atomic diffusion processes are enhanced for the resultant LS species with smaller atomic volume. This facilitates the subsequent *Cmcm* → *Pmma* disorder/order transition in the sublattice of sixfold coordinated sites.

The temperature dependence of the resistance measured to a highest pressure of ~68 GPa indicates continued activated transport processes [linearity in $\ln(R)$ vs $1/T$] similar to the preceding *Cmcm* structural regime. The charge gap ($E_g = 2E_a$) deduced from fits to the linearized data in the inset of Fig. 5 is $E_g \sim 120$ meV at ~68 GPa. The pressure dependence of the resistance at RT to much higher pressure shows a plateau behavior from ~68 GPa onwards up to ~80 GPa. This suggests that the sample remains nonmetallic to the highest pressure of this study, i.e., to near a megabar.

IV. SUMMARY AND CONCLUSIONS

We arrive at the following conclusions on the pressure response of the magnetic-electronic behavior of ulvöspinel Fe_2TiO_4 and its relation to structural transformation and electrical-transport behavior:

(i) The cubic-to-tetragonal transition rises from $T_{\text{J-T}} \sim 163$ K to RT by ~8 GPa, after which tetragonality at RT prevails until ~16 GPa when a new structural transition is onset. Complex magnetic spectra occur, reflecting levels of disorder in the Fe/Ti B sublattice. Throughout this pressure range, there is a large average H_{hf} distribution component designated HS(VI-2), corresponding to a certain degree of cation segregation and highly asymmetric Fe local environments (large QS). In addition, two different smaller average H_{hf} distribution components also occur. These are related to a different degree of Fe/Ti segregation at HS(VI-1)-designated sixfold coordinated sites and to fourfold coordinated sites designated HS(IV).

(ii) The tetragonal spinel transforms to the orthorhombic post-spinel in the range 16–20 GPa as discerned in the precipitous ∼8% decrease in unit-cell volume and decrement by two orders of magnitude of the RT resistance. The post-spinel is identified to be of the $CaTi_2O_4$ type with SG *Cmcm*, in accord with previous work. This seems to only have had minor effects on the HI parameters and magnetic behavior across the structural transition. Small average H_{hf} [HS(VI-1)] and large average H_{hf} [HS(VI-2)] categories of sixfold coordinated sites prevail. Tetrahedral sites transform to higher (eightfold) coordinated, HS(VIII)-designated sites with a small average H_{hf} and other similar HI parameters to HS(IV) sites. All of this perpetuates to 40–45 GPa when a change to a steeper pressure dependence of unit-cell volume occurs. This leads to a ∼3.5% change in unit cell volume, and $P \sim 50$ GPa is identified as another phase transition region.

(iii) In the vicinity of ∼50 GPa, changes are discerned in RT and LT MS spectra compared to those typical of the HS state of the *Cmma* phase. Magnetic spectra down to liquid helium temperatures comprise large average $H_{hf} \sim 42$ T contributions and a diamagnetic central doublet. This doublet is maximally ∼25% of the Fe sites from the analysis of spectra collected at higher pressures. The HI parameters of the doublet have IS and QS values typical of a LS state. This evolves from the highly distorted HS(VI-2) sites and comprises about half of the sixfold coordinated Fe sites in the lattice. The rest of the Fe locations have large average $H_{hf} \sim 42$ T values, which signify quenching of orbital moment contributions at HS(VI-1) and HS(VIII) sites. These findings are in contrast to previous claims of spin crossover initiating as low as ∼14 GPa [17]. Indeed spin crossover does occur, but only at specific sixfold coordinated sites, and it initiates beyond 40 GPa within the *Cmcm* phase. The relatively small volume change of ∼3.5% across the spin-crossover regime is considered corroboration of only partial conversion of sixfold coordinated Fe sites to the LS state.

(iv) At pressures beyond ∼55 GPa, XRD profiles indicate symmetry lowering to the *Pmma* subgroup supposed to be associated with Fe/Ti order at sixfold coordinated sites. Partial spin crossover initiated in the preceding *Cmcm* phase facilitates a subsequent disorder/order transition to the *Pmma* phase in the vicinity of ∼55 GPa. Analysis of the MS spectra indicates that the partial spin crossover, limited to the highly distorted sixfold coordinated sites of ∼25% abundance, persists up to ∼90 GPa in the *Pmma* phase.

(v) Arrhenius activated nearest neighbor hopping is applicable to the compound across all structural transition boundaries. The RT resistance tends to a plateau at pressures beyond ∼55 GPa. The charge gap is inferred to be ∼100 meV in the range 80–90 GPa, based on the behavior of the resistance at RT and pressure dependence of activation energies obtained at lower pressures.

Thus, the very high-pressure post-spinel phase of Fe_2TiO_4 at 55–90 GPa is nonmetallic, is stabilized in the *Pmma* structure involving Fe/Ti ordered in sixfold coordinated sites, and has a partially spin-converted lattice involving LS states at ∼25% of the Fe sites. The remainder of the six- and eightfold coordinated Fe sites have magnetic ground states in which the orbital moment is quenched, to yield spin-only internal magnetic field values of ∼42 T.

Our XRD pressure measurements to above 80 GPa, well beyond the maximum pressure of previous papers, indicate that that there is a ∼33% reduction in unit-cell volume to these extremes, yet the presumably appreciable 3*d* band broadening associated with such densification is not sufficient to disrupt strong electron correlations and close the charge gap. The effective onsite repulsion parameter (U_{eff} determining the gap between upper and lower Hubbard bands) renders the nonmetallic (Mott insulator type) behavior to these partially filled 3*d* band oxides. In the HS $3d^6(Fe^{2+})$ configuration, U_{eff} is constant as a function of pressure and increases at spin crossover in sixfold coordinated sites [46]. Moreover, the high-pressure *Pmma* structure involves ordered Fe and Ti at sixfold coordinated sites. Ti^{4+} has an empty 3*d* band and should therefore be able to accommodate a charge carrier in a delocalization process because there would be no energy cost U_{eff} from double occupation at Ti sites. We therefore infer that it is the *Cmcm* (disorder) → *Pmma* (order) transition and resultant Fe/Ti ordered configuration which does not render sufficient Fe-Ti orbital overlap for delocalization to occur. In addition, the disposition of LS sites throughout the lattice with increased U_{eff} values in only quarter of the Fe sites, is sufficient to ensure that the cost of double occupation (onsite Coulomb repulsion) continues to supersede the kinetic energy gained in band broadening and associated delocalization. As such, strong electron correlations prevail in the atomically ordered *Pmma* phase of nonmetallic Fe_2TiO_4, in spite of appreciable 3*d* band broadening at high density.

ACKNOWLEDGMENTS

We acknowledge with gratitude the receipt of the Fe_2TiO_4 sample from X. Wu (School of Earth and Space Sciences, Peking University). We also acknowledge professional assistance from Rudolph Rüffer, Aleksandr Chumakov, and support staff during the synchrotron Mössbauer source measurements at the ID-18 beamline of the ESRF. This research was supported by the Israel Science Foundation (Grant No. 1189/14). G.R.H. acknowledges financial support from the National Research Foundation of South Africa (Grant No. 105870).

---

[1] T. Yamanaka, T. Mine, S. Asogawa, and Y. Nakamoto, Phys. Rev. B **80**, 134120 (2009).
[2] S. Nakamura and A. Fuwa, Hyperfine Interact. **226**, 267 (2014).
[3] Y. Ishikawa and Y. Syono, J. Phys. Soc. Jpn **31**, 461 (1971).
[4] Y. Ishikawa and Y. Syono, Phys. Rev. Lett. **26**, 1335 (1971).
[5] M. Kataoka, J. Phys. Soc. Japan **36**, 456 (1974).
[6] N. Church, J. Feinberg, and R. J. Harrison, Geochem., Geophys., Geosyst. **12**, Q07Z27 (2011).
[7] R. J. Harrison, E. J. Palin, and N. Perks, Am. Mineral. **98**, 698 (2013).

[8] D. J. Dunlop and Ö. Özdemir, *Rock Magnetism. Fundamentals and Frontiers* (Cambridge University Press, Cambridge, 1997).

[9] J. Klerk, V. A. M. Brabers, and A. J. M. Kuipers, J. Phys. Colloques **38**(C1), C1-187 (1977).

[10] Z. Kąkol, J. Sabol, and J. M. Honig, Phys. Rev. B **43**, 649 (1991).

[11] K. Glazyrin, C. McCammon, L. Dubrovinsky, M. Merlini, K. Schollenbruch, A. Woodland, and M. Hanfland, Am. Mineral. **97**, 128 (2012).

[12] W. M. Xu, G. Yu. Machavariani, G. Kh. Rozenberg, and M. P. Pasternak, Phys. Rev. B **70**, 174106 (2004).

[13] E. R. Morris and Q. Williams, J. Geophys. Res. **102**, 18139 (1997).

[14] L. S. Dubrovinsky, N. A. Dubrovinskaia, C. McCammon, G. Kh. Rozenberg, R. Ahuja, J. M. Osorio-Guillen, V. Dmitriev, H.-P. Weber, T. L. Bihan, and B. Johansson, J. Phys.: Condens. Matter **15**, 7697 (2003).

[15] Y. Ding, D. Haskel, S. G. Ovchinnikov, Y.-C. Tseng, Y. S. Orlov, J. C. Lang, and H.-k. Mao, Phys. Rev. Lett. **100**, 045508 (2008).

[16] D. Errandonea, in *Pressure-Induced Phase Transitions in AB_2X_4 Chalcogenide Compounds*, Springer Series in Materials Science, edited by F. J. Manjón, I. Tiginyanu, and V. Ursaki (Springer-Verlag, Heidelberg, 2014), Vol. 189, pp. 53–73.

[17] T. Yamanaka, A. Kyono, Y. Nakamoto, Y. Meng, S. Kharlamova, V. V. Struzhkin, and H.-k. Mao, Am. Mineral. **98**, 736 (2013).

[18] Á. M. Arévalo-López, A. J. Dos-santos-García, E. Castillo-Martínez, A. Durán, and M. Á. Alario-Franco, Inorg. Chem. **49**, 2827 (2010).

[19] A. Kyono, M. Ahart, T. Yamanaka, S. Gramsch, Ho-Kwang Mao, and R. J. Hemley, Am. Mineral. **96**, 1193 (2011).

[20] W. M. Xu, G. R. Hearne, S. Layek, D. Levy, J.-P. Itié, M. P. Pasternak, G. Kh. Rozenberg, and E. Greenberg, Phys. Rev. B **95**, 045110 (2017).

[21] Y. Wu, X. Wu, and S. Qin, J. Sol. State Chem. **185**, 72 (2012).

[22] T. Yamanaka, A. Uchida, and Y. Nakamoto, Am. Mineral. **93**, 1874 (2008).

[23] G. R. Hearne, M. P. Pasternak, and R. D. Taylor, Rev. Sci. Inst. **65**, 3787 (1994).

[24] V. Potapkin, A. I. Chumakov, G. V. Smirnov, J.-P. Celse, R. Rüffer, C. McCammon, and L. Dubrovinsky, J. Synchrotron Rad. **19**, 559 (2012).

[25] The HI parameters including Fe site abundances are derived from fitting the spectral envelope with Lorentzian subcomponents. The IS (chemical shift) is proportional to the s-electron density at the Fe nucleus and is influenced by d-electron shielding. The quadrupole doublet-splitting or line shift, QS, is proportional to the deviation from cubic symmetry of both the surrounding electron configuration and nearest neighbor atoms. The IS, QS, and H_{hf} (from magnetically split hyperfine structure) parameters have distinct “fingerprint” values for both valences and spin states of $Fe^{2+}(3d^6)$ and $Fe^{3+}(3d^5)$. In complex spectra, with appreciable overlap of subcomponents, mainly IS and to a lesser extent H_{hf} values of fitted subspectra are obtained with good reliability, to establish the electronic state of the Fe.

[26] For example, MossWinn 4.0 by Zoltán Klencsár (see http://www.mosswinn.com/).

[27] G. Yu. Machavariani, M. P. Pasternak, G. R. Hearne, and G. Kh. Rozenberg, Rev. Sci. Instrum. **69**, 1423 (1998).

[28] D. Errandonea, R. Boehler, S. Japel, M. Mezouar, and L. R. Benedetti, Phys. Rev. B **73**, 092106 (2006).

[29] S. Klotz, J. C. Chervin, P. Munsch, and G. L. Marchand, J. Phys. D: Appl. Phys. **42**, 075413 (2009).

[30] A. P. Hammersley, S. O. Svensson, M. Hanfland, A. N. Fitch, and D. Hausermann, High Press. Res. **14**, 235 (1996).

[31] A. P. Hammersley, ESRF Internal Report No. ESRF97HA02T, “FIT2D: An Introduction and Overview”, (1997). See http://www.esrf.eu/computing/scientific/FIT2D/.

[32] C. Prescher and V. B. Prakapenka, High Press. Res. **35**, 223 (2015).

[33] B. H. Toby and R. B. Von-Dreele, J. Appl. Cryst. **46**, 544 (2013).

[34] G. S. Pawley, J. Appl. Cryst. **14**, 357 (1981).

[35] A. D. Chijioke, W. J. Nellis, A. Soldatov, and I. F. Silvera, J. Appl. Phys. **98**, 114905 (2005).

[36] A. Dewaele, F. Datchi, P. Loubeyre, and M. Mezouar, Phys. Rev. B **77**, 094106 (2008).

[37] The quadrupole doublet-splitting or line shift, QS, is proportional to the deviation from cubic symmetry of both the surrounding electron configuration and nearest neighbor atoms. The QS is half the value of the quadrupole coupling $e^2q_{zz}Q$, where $eq_{zz} \equiv V_{zz}$ is the maximum value of the EFG from the site asymmetry and Q is the quadrupole moment.

[38] R. Vanleerberghe and R. E. Vandenberghe, Hyperfine Interact. **23**, 75 (1985).

[39] K. Ôno and L. Chandler, J. Phys. Soc. Japan **25**, 174 (1968).

[40] Extrinsic sources of line broadening emanate from the high specific activity of the source and from pressure gradients and nonhydrostatic pressure effects in the sample cavity. These are not easily deconvoluted from intrinsic broadening effects from a distribution of Fe local environments. As such, it may be difficult to find a reliable and unique parameter distribution. Various trial fits, for example, using QS or H_{hf} distributions, have shown that the average values of these distributions are quite reliable and conform closely to those obtained when discrete broadened Lorentzian subcomponents are fitted. The parameter distributions are thus mimicked by the line broadening which includes extrinsic as well as intrinsic contributions.

[41] The magnetic hyperfine field is a result of the nuclear Zeeman splitting of ^{57}Fe nuclear levels due to an internal magnetic field at the nucleus. The primary contribution to this internal field H_{hf} is from the contact term. This is the effect of d-electron spin polarization on the s electrons. Other contributions to H_{hf} are from comparatively small dipolar and orbital terms. In HS ferric iron, the orbital and dipolar terms are negligibly small. The orbital term in HS ferrous iron and LS ferric iron may be appreciable and of opposite sign to the contact term. At well below the magnetic ordering temperatures, H_{hf} in HS ferric oxides is typically clustered around ∼50 T, whereas in ferrous compounds, it may range from near zero to 44 T depending on the orbital configuration.

[42] F. E. Mabbs and D. J. Machin, *Magnetism and Transition Metal Complexes* (Dover, New York, 2008).

[43] For an unquenched orbital angular momentum contribution, there must be: degeneracy of $3d$ levels, an unoccupied level, and an orbital must be able to transform to another level by rotation, e.g., d_{xz} and d_{yz}. Quenching ensues when these conditions are violated. It may be due to a polyhedral distortion and associated CF evolution which results in a lifting of $3d$ degeneracies.

[44] The IS has the formulation IS $= -(\text{constant})\rho_s(0) + (\text{constant}')$, where the constants are atomic and nuclear parameters. In this formulation, $\rho_s(0)$ is the s-electron density at the nucleus. This indicates that IS decreases as the s-electron density increases under compression.

[45] There is a corresponding increased energy cost of occupying higher-lying e_g electronic states, which are originally separated from lower-lying t_{2g} orbital levels by the CF splitting designated CF $= 10Dq$ ($\sim$1 eV). At a critical value of the CF splitting, this increased cost will supersede the energy gain from maximizing the possible pairs of parallel spins in different $3d$ orbitals on the same site (Hund's rule, whereby there is effectively a gain of $-J \sim -1$ eV for each set of parallel spins, from intra-atomic "onsite" ferromagnetic exchange coupling). When CF $> 3J$ for the $3d^6(\text{Fe}^{2+})$ electronic configuration, antiparallel spin pairing in lower-lying (t_{2g}) electronic orbital states becomes energetically favorable, and HS → LS crossover occurs.

[46] S. G. Ovchinnikov, J. Exp. Theor. Phys. **107**, 140 (2008).

[47] P. Gütlich, E. Bill, and A. X. Trautwein, *Mössbauer Spectroscopy and Transition Metal Chemistry: Fundamentals and Applications* (Springer, Berlin, 2011).

[48] J.-F. Lin, S. Speziale, Z. Mao, and H. Marquardt, Rev. Geophys. **51**, 244 (2013).

[49] According to R. D. Shannon, Acta Crystallogr., Sect. A **32**, 751 (1976), the ionic radii at ambient conditions of Fe^{2+} in sixfold coordination in HS and LS states are 0.78 and 0.61 Å, respectively.

[50] M. Merlini, M. Hanfland, M. Gemmi, S. Huotari, L. Simonelli, and P. Strobel, Am. Mineral. **95**, 200 (2010).

[51] K. Glazyrin, N. Miyajima, J. S. Smith, and K. K. M. Lee, J. Geophys. Res. Solid Earth **121**, 3377 (2016).

[52] H. Hsu, K. Umemoto, P. Blaha, and R. M. Wentzcovitch, Earth Planet. Sci. Lett. **294**, 19 (2010).

[53] F. Birch, J. Geophys. Res. **83**, 1257 (1978).

[54] J. K. Burdett, R. Hoffmann, and R. C. Fay, Inorg. Chem. **17**, 2553 (1978).